

Dynamic regional divergence of SV2A expression in a mouse model of primary tauopathy: A longitudinal multi-tracer PET study

Yunlei Li^a, Artem Zatcepin^{a,b}, Giovanna Palumbo^a, Rosel Oos^a, Karin Wind-Mark^a, Simon Lindner^a, Franz-Josef Gildehaus^a, Johannes Gnörich^{a,c,d}, Rudolf A Werner^{a,e}, Matthias Brendel^{a,c,d,*}, Lea H Kunze^{a,c}

^a Department of Nuclear Medicine, LMU University Hospital, LMU Munich, 81377 Munich, Germany

^b Department of Nuclear Medicine, Hannover Medical School, 30625 Hannover, Germany

^c German Center for Neurodegenerative Diseases (DZNE), 81377 Munich, Germany

^d Munich Cluster for Systems Neurology (SyNergy), 81377 Munich, Germany

^e Russell H. Morgan Department of Radiology and Radiological Sciences, Johns Hopkins School of Medicine, Baltimore 21287 Maryland, United States

ARTICLE INFO

Keywords:

Synaptic density

SV2A-PET

Tau

Desynchronization

ABSTRACT

In tauopathies, tau accumulation and neuroinflammation are associated with progressive synaptic and network alterations that contribute to neurodegeneration. We used 8 PS19 and 12 C57Bl/6 (WT) mice undergoing consecutive [¹⁸F]UCB-H PET scans between 5.7 and 11.0 months of age to longitudinally evaluate SV2A expression levels, with terminal validation via immunohistochemistry. A desynchronization index (DI) quantified deviation from a reference-derived inter-regional SV2A expression pattern from whole-brain SV2A-PET data, and principal component analysis (PCA) further summarized these regional deviation profiles. Baseline translocator protein (TSPO), [¹⁸F]GE-180 and monoamine oxidase B (MAO-B, [¹⁸F]F-DED) imaging for activated microglia and reactive astrogliosis were performed to detect early neuroinflammation, which was subsequently correlated with serial SV2A expression, evaluated by the area under the curve (AUC) of [¹⁸F]UCB-H z-scores (PS19 vs. WT). We observed phased SV2A expression alterations in PS19 mice in the neocortex, hippocampus CA1, brainstem, thalamus, hypothalamus, and cerebellum, showing an increasing trend from 8.4 to 10.0 months of age (+8.1% ± 3.0%), followed by a rapid decline towards 11.0 months of age (-18.4% ± 4.7%), together with greater later-stage inter-regional SV2A expression pattern deviation. Tau burden tended to show a broadly negative association with SV2A expression levels across primary and exploratory regions. Associations of SV2A-PET signal variation with early microglial activation and reactive astrogliosis differed between PS19 and WT mice. In summary, these findings suggest that longitudinal [¹⁸F]UCB-H PET may provide a feasible approach for tracking stage-dependent regional SV2A expression alterations and inter-regional deviation in this mouse model of primary tauopathy.

1. Introduction

Neurodegenerative diseases (NDDs) are a heterogeneous group of chronic progressive diseases (Wilson et al., 2023). Alzheimer's disease (AD) is one of the most widespread NDDs. The main characteristics of AD can be explained by a simplified A-T-N pathological model, which constitutes that β -amyloid (A β) aggregation is followed by tau protein accumulation, and ultimately leads to neurodegeneration (Jack et al., 2018). Recent research finds that A β is a pathological catalyst, accelerating disease progression by enhancing the hyperconnectivity of the

brain and paving the way for the rapid spread of tau pathological proteins (Roemer-Cassiano et al., 2025). Regional tau burden is more closely related to neural network dysfunction and is independent of A β plaque deposition (Wang et al., 2024). The critical pathogenic role of tau pathology in NDDs is becoming increasingly clear. Among the six specific isoforms of tau protein, 1N4R tau is identified as the core toxic factor, with higher phosphorylation levels, leading to a significant decrease in neuronal resistance and increased vulnerability (Buchholz et al., 2025). In addition, a series of tauopathies such as progressive supranuclear palsy (PSP), corticobasal degeneration (CBD), and

* Corresponding author at: Matthias Brendel, Department of Nuclear Medicine, University Hospital, LMU Munich, Marchioninstr. 15, 81377 Munich, Germany.
E-mail address: Matthias.Brendel@med.uni-muenchen.de (M. Brendel).

<https://doi.org/10.1016/j.neuroimage.2026.121932>

Received 2 December 2025; Received in revised form 13 April 2026; Accepted 14 April 2026

Available online 15 April 2026

1053-8119/© 2026 The Author(s). Published by Elsevier Inc. This is an open access article under the CC BY license (<http://creativecommons.org/licenses/by/4.0/>).

frontotemporal dementia (FTD) are also associated with tau hyperphosphorylation as the primary pathological feature (Chung et al., 2021).

Neuroinflammation, characterized by activated microglia and reactive astrocytes, acts both as a neuroprotective mechanism, participating in debris and pathogen clearance, suppressing injury, initiating healing, and shaping neural circuits (Salter and Beggs, 2014, Hickman et al., 2018, Vainchtein and Molofsky, 2020, Jha et al., 2018), and as a neurotoxic process that promotes neurodegeneration under the sustained stimulation of protein aggregates (Han et al., 2024, Heneka et al., 2024). In addition, astrocytes are an important component of the tri-synaptic network, involved in maintaining glutamate homeostasis, and may directly cause synaptic defects by releasing extracellular factors (Jha et al., 2018, Liu et al., 2021). Meanwhile, ample evidence suggests that excessive activation of neuroinflammation is not merely a consequence of pathological protein stimulation but leads to protein aggregation in the early stages (Hong et al., 2016, Sosna et al., 2018, Zhang et al., 2023).

Synaptic loss in NDDs is associated with reduced functional connectivity in brain regions and acts as a major pathological factor that worsens cognitive impairment via neural network dysfunction (Mecca et al., 2022, Whiteside et al., 2023). Synaptic vesicle protein 2A (SV2A) participates in synaptic homeostasis regulation and is widely expressed at the membrane of synaptic vesicles in the terminal boutons (Rossi et al., 2022, Kwon and Chapman, 2012, Bajjalieh et al., 1992). Based on this, positron emission tomography (PET) targeting SV2A demonstrates excellent potential for visualization of SV2A changes in vivo (Finnema et al., 2016, Toyonaga et al., 2022, Ullrich Gavilanes et al., 2025). Clinical studies show that AD patients exhibit significantly reduced SV2A-PET uptake in the medial and lateral temporal lobes and neocortex compared to healthy controls (Wang et al., 2024, Mecca et al., 2020). Globally lower SV2A expression is also found in PSP and CBD patients, even in brain regions without significant grey matter atrophy (Holland et al., 2020). However, the prolonged disease course and progressive deterioration characteristic of NDDs limit the ability of cross-sectional SV2A-PET studies to capture the temporal changes in SV2A expression, thereby making longitudinal assessment in disease models essential. To assess the longitudinal variation in SV2A expression levels and their connection with neuroinflammatory processes, we conducted longitudinal [^{18}F]UCB-H PET scans using PS19 mice as a model of tauopathy and age-matched wild-type controls, along with baseline translocator protein (TSPO, [^{18}F]GE-180) PET scans targeting activated microglia and monoamine oxidase B (MAOB, [^{18}F]F-DED) PET scans targeting reactive astrogliosis. Moreover, we applied desynchronization index-based analysis of SV2A expression to assess the inter-regional deviation pattern at different stages. Finally, terminal immunohistochemistry was performed to validate the SV2A-PET results. We hypothesize that [^{18}F]UCB-H PET may enable tracking of longitudinal SV2A expression level alterations and inter-regional pattern deviation during the progression of tau pathology, and may help explore their relationships with tau deposition and early neuroinflammation.

2. Materials and methods

2.1. Animals and study design

The preclinical experiments were approved by the local animal care committee of the Government of Upper Bavaria (Regierung Oberbayern, approval number: ROB-55.2-2532.Vet_02-19-26) and were conducted in accordance with the National Guidelines for Animal Protection, Germany, overseen by a veterinarian. All experiments complied with the ARRIVE guidelines and the U.K. Animals (Scientific Procedures) Act, 1986, and associated guidelines, EU Directive 2010/63/EU for animal experiments. Animals were housed in a temperature- and humidity-controlled environment with a 12 h light–dark cycle, with free access to chow (Sniff Spezialdiaeten GmbH, Soest, Germany) in standard

pellets and water.

The PS19 transgenic mouse model (JAX stock #024841) expresses the P301S mutant form of human microtubule-associated protein tau with one N-terminal insert and four microtubule binding repeats (1N4R), driven by the mouse prion promoter (*Prnp*) (Yoshiyama et al., 2007). PS19 mice develop hyperphosphorylated tau in the entorhinal cortex and hippocampus by 3 months of age, followed by neurofibrillary tangles (NFTs) in the prefrontal cortex and hippocampus at 6 months of age, with progressive accumulation. By 9 months of age, they exhibit motor deficits and increased frailty, and present with paralysis, inability to feed, and severe weight loss at 10 months of age (Yoshiyama et al., 2007). 8 female PS19 mice and 12 female age-matched C57Bl/6 controls underwent longitudinal PET scans as described in Fig. 1 (created in BioRender. Li, Y. (2026) <https://BioRender.com/ro290l>). Technical problems with scan acquisition or an insufficient amount of injected radiotracer activity concentration for a few mice led to variations in cohort size. These outliers were excluded, but sufficient data points were retained for analysis. Four mice from each cohort were randomly selected for immunohistochemistry to validate the [^{18}F]UCB-H PET results after the final scan. Mice were deeply anaesthetized and transcardially perfused with phosphate buffered saline (PBS). Brains were harvested and fixed in 4% paraformaldehyde at 4°C for 10 h. Then, brains were stored at 4°C in PBS containing 0.02% Na_3N until preparation for staining.

2.2. PET imaging

Radiochemistry, PET image acquisition, and image pre-processing followed previously established protocols (Vogler et al., 2023, Ballweg et al., 2023, Brendel et al., 2016). Briefly, mice were anesthetized with isoflurane before being injected with an average dose of 14.8 ± 1.6 MBq [^{18}F]UCB-H, 10.2 ± 2.3 MBq [^{18}F]F-DED, and 13.1 ± 1.2 MBq [^{18}F]GE-180. Imaging was performed dynamically 0–60 min p.i. on the Mediso NanoScan PET/CT 0–60. In between PET scans at baseline (5.7 months of age), the mice were resting for at least two days.

2.3. PET image analysis

PET image analysis was performed in PMOD (version 3.5, PMOD Technologies, Zurich, Switzerland) as described previously (Overhoff et al., 2016). In brief, images were spatially normalized to a template and subsequently adjusted to the injected activity and the weight of each animal by calculating a standardized uptake value (SUV) (Pike, 2009). Based on evidence that spontaneous tau pathology in PS19 mice propagates along brain networks and progressively involves neocortex, hippocampus, limbic system, and subcortical regions (Ramirez et al., 2025), we a priori defined the neocortex (92 mm^3), hippocampus CA1 (5 mm^3), hippocampus CA3 (7 mm^3), amygdala (12 mm^3), brainstem (12 mm^3), thalamus (27 mm^3), hypothalamus (10 mm^3), and cerebellum (12 mm^3) as eight primary hypothesis-driven volumes of interest (VOIs). The entorhinal cortex (10 mm^3), piriform cortex (9 mm^3), visual cortex (8 mm^3), auditory cortex (7 mm^3), motor cortex (20 mm^3), somatosensory cortex (16 mm^3), and olfactory cortex (22 mm^3) were additionally included as seven exploratory cortical subregions to investigate potential uptake differences within the neocortex and to provide more detailed cortical uptake data. The respective VOIs were defined from the Ma-Benveniste-Mirrione atlas aligned on a T1 weighted magnetic resonance imaging (T1 MRI) template (Ma et al., 2005, Gnorich et al., 2023). To verify the results obtained for the SUV data, we performed an additional analysis using volume-of-distribution (V_T) images based on the image-derived input function (IDIF) in PMOD, according to a previously described method for [^{18}F]UCB-H PET scans, as a tissue-independent image analysis (Logan et al., 1990). Therefore, we created a spherical VOI with a radius of 2.5 mm in the heart to obtain the blood input curve and controlled the maximum error tolerance to 10% between data points and the regression line with a threshold of 0% to retain all pixels

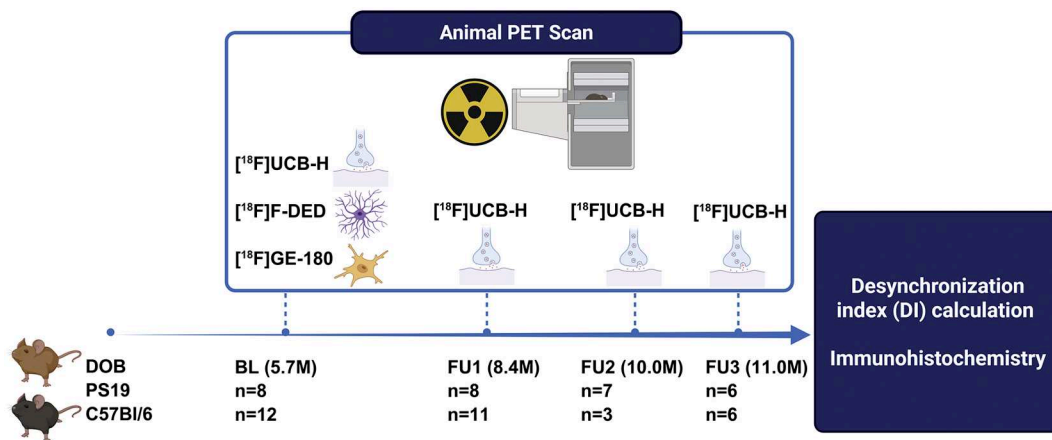


Fig. 1. The flow chart shows the study design. [¹⁸F]UCB-H PET scans were performed at 5.7, 8.4, 10.0, and 11.0 months of age, [¹⁸F]F-DED and [¹⁸F]GE-180 PET scans were performed at 5.7 months to assess baseline reactive gliosis. For additional PET-data analysis, the desynchronization index (DI) was calculated for each brain region. After the last PET-scan at 11.0 months of age, mice were perfused and four mice from each cohort were randomly selected for terminal immunohistochemical analysis. Abbreviations: BL, baseline; FU, follow-up; DI, desynchronization index.

when modeling dynamic imaging data (Vogler et al., 2023). The thus obtained PET-data, both SUV and V_T , was transformed to z-scores. In addition, we calculated the area under the curve (AUC) of [¹⁸F]UCB-H SUV z-scores to reflect the SV2A expression levels variation in PS19 and C57Bl/6 mice from 8.4 to 11.0 months.

For [¹⁸F]UCB-H voxel-wise comparisons between PS19 and C57Bl/6 mice, we performed statistical parametric mapping (SPM) analysis (SPM12, 2016, Wellcome Department of Cognitive Neurology, London, UK) implemented in Matlab (MATLAB, 2016) (Brendel et al., 2016). Therefore, a two-sample t-test was performed in SPM to compare the [¹⁸F]UCB-H uptake differences between cohorts at each time point (independence of groups; unequal variance). No grand mean scaling and masking were applied. SPM results were displayed at a voxel-wise threshold of $p < 0.05$ (uncorrected) with no extent threshold applied and no correction for multiple comparisons; thus, voxel-wise findings were considered exploratory.

2.4. Synaptic activity desynchronization index

We calculated the Desynchronization Index (DI), a quantitative score, to assess the SV2A expression level synchronization of the PS19 and C57Bl/6 mice in longitudinal and horizontal comparisons at the individual level (Zatcepin et al., 2024). All calculations were performed using a custom-made Python script (Numpy and Pandas libraries). Briefly, an additional group of 5.3 months old C57Bl/6 mice that underwent [¹⁸F]UCB-H scan was first used as a reference cohort ($n = 37$) and mean [¹⁸F]UCB-H SUV values of all target VOIs were extracted. Using these values, we calculated a linear fit between each VOI pair (mean of 10000 bootstraps). Next, we extracted mean [¹⁸F]UCB-H SUV values of the PS19 and C57Bl/6 mice from 5.7 to 11.0 months of age. For each individual subject and each VOI pair, we calculated the perpendicular distance from that subject's pair of values to the corresponding reference linear fit. Finally, to obtain the DI of a particular VOI, we summed up all the perpendicular distances of all the VOI pairs that included that VOI.

2.5. Immunohistochemistry

Terminal immunohistochemistry was performed to assess SV2A expression level and tau accumulation, validating the [¹⁸F]UCB-H PET results. The left sagittal hemisphere of four randomly selected mice per group was cut into 50 μ m thick slices using a vibratome (VT1200S, Leica, Germany). Then, we performed free-floating staining of the sections as previously described (Vogler et al., 2023, Xiang et al., 2021,

Kunze et al., 2025). To this end, two lateral and two medial slices from each mouse were incubated at 4°C overnight in PBS with 0.5% Triton X100 and 5% normal goat serum (NGS) containing rabbit polyclonal anti-SV2A primary antibody (1:500, Synaptic Systems, 119002), chicken polyclonal anti-NeuN primary antibody (1:500, Sigma-Aldrich, ABN91), and mouse monoclonal anti-AT8 primary antibody (1:1000, Thermo Fisher, MN1020). Furthermore, all slices were incubated for 2 h at room temperature with suitable secondary antibodies.

Image acquisition was performed with the THUNDER Imager Tissue (Leica Microsystems CMS GmbH, Wetzlar, Germany). The target regions involved the neocortex, hippocampus CA1, hippocampus CA3, and brainstem for quantifying SV2A signal in the NeuN area coverage. The target regions were acquired with a $\times 63$ oil objective, and the z-stack consisted of 19 slices with a 0.27 μ m step size, covering a total depth of 5 μ m. In addition, we also acquired the overview images stained with NeuN and AT8 by using a $\times 10$ objective. In each slice, 2-3 fields of view for each region with equal distribution were selected for zoom-in with a $\times 20$ objective, and the z-stack consisted of 8 slices with a 0.57 μ m step size, covering a total depth of 5 μ m. The LAS X Software (version 3.9.1.28433) was used for image pre-processing. Image analysis was performed on 16-bit images using ImageJ (version 1.54k) (Schindelin et al., 2012) by quantifying the area above a threshold of 35 for assessing SV2A in NeuN+ area coverage (%Area) and by quantifying the area above a threshold of 20 for assessing AT8+ coverage (%Area).

2.6. Statistics

Statistical analysis of PET and immunohistochemical data was performed using GraphPad Prism (version 10.1.2 for Windows, GraphPad Software, San Diego, CA, USA). Unless otherwise stated, all statistical tests were two-tailed. To define the scope of multiple comparisons, the eight primary VOIs and the seven exploratory cortical subregions were treated as two independent families of tests. Multiple comparisons were controlled using the Benjamini-Hochberg false discovery rate (BH-FDR) correction ($q = 0.05$) within corresponding families of tests. Results with q value (BH-FDR-adjusted p value) < 0.05 were considered statistically significant, whereas results that did not survive correction were interpreted descriptively and reported as trends or exploratory findings. Effect sizes were reported as partial eta-squared (η^2) for mixed-effects models and one-way ANOVA, and as Cohen's d for pairwise comparisons. For mixed-effects models, we additionally reported conditional R^2 as a model-level index of explained variance.

Longitudinal group differences for [¹⁸F]UCB-H SUV and V_T z-score were statistically evaluated by a two-way mixed-effects model (fixed

effects: genotype, time, and genotype \times time; random intercept: individual animal). The primary inferential test was the genotype \times time interaction, used to assess longitudinal uptake trajectory differences between PS19 and C57Bl/6 mice.

To characterize phase-specific features of changes in [^{18}F]UCB-H uptake, three adjacent intervals based on the scan time points were defined (5.7-8.4 months of age, 8.4-10.0 months of age, and 10.0-11.0 months of age). In PS19 mice, the slopes of the different time intervals of [^{18}F]UCB-H SUV z-scores were treated as repeated measures outcomes to test the overall interval effect using a one-way mixed-effects model (fixed effects: time; random intercept: individual animal). Pre-defined adjacent interval comparisons were then performed to localize the timing and direction of slope changes as pre-specified contrasts in the same mixed effects model.

An unpaired t-test was applied to examine the differences between PS19 and C57Bl/6 mice at 11.0 months of age in [^{18}F]UCB-H uptake, SV2A expression levels in the NeuN+ area, and tau accumulation with AT8+.

Pearson's correlation coefficient was used to determine the association between [^{18}F]UCB-H uptake and tau accumulation at 11.0 months of age, as well as the association between SV2A expression level variation degrees and baseline reactive gliosis. Spearman correlation was performed when the data did not follow a Gaussian distribution.

The DI differences between genotypes at different time points were

assessed by unpaired t-tests. Raw p-values from these tests were subsequently BH-FDR adjusted ($q = 0.05$), treating all genotype comparisons across all time points within the corresponding VOI as a single family of tests. Principal component analysis (PCA) was performed based on VOIs showing significant DI differences between PS19 and C57Bl/6 mice at 10.0 or 11.0 months after BH-FDR correction, and the first principal component (PC1) was compared across groups using one-way ANOVA, followed by unpaired t-tests with BH-FDR correction across all pairwise comparisons. These statistical processes were performed using Python 3.7 (Scikit-learn library).

3. Results

3.1. [^{18}F]UCB-H PET signal increase before it decreases in most brain regions in PS19 mice

A significant genotype \times time interaction was observed for SV2A expression levels as measured by [^{18}F]UCB-H SUV z-scores in the neocortex ($q = 0.047$) and hippocampus CA3 ($q = 0.022$), surviving BH-FDR correction across the eight primary VOIs, indicating differential longitudinal changes between PS19 and C57Bl/6 mice (Figs. 2B, 3B and Supplemental Table 1). In exploratory analyses of cortical subregions, a significant genotype \times time interaction was also observed in the entorhinal cortex ($q = 0.041$) and somatosensory cortex ($q = 0.037$) after

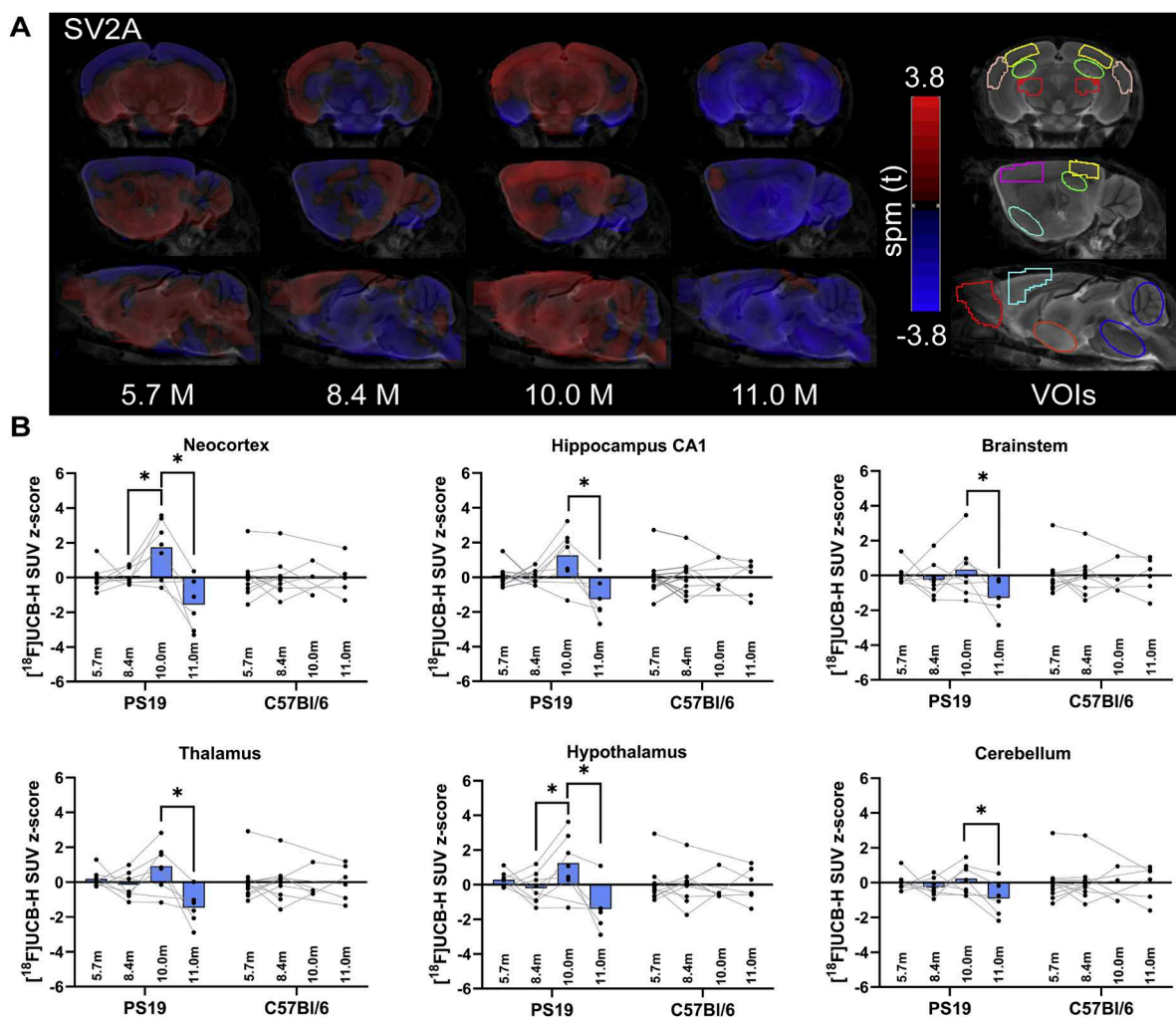


Fig. 2. (A) SPM images show differences in SV2A expression level between PS19 and C57Bl/6 mice in the neocortex, hippocampus CA1, brainstem, thalamus, hypothalamus, and cerebellum at 5.7, 8.4, 10.0, and 11.0 months of age, with a substantial increase (depicted in red) before a decrease (depicted in blue) in PS19 mice. The coronal and sagittal planes of target VOIs are projected on a mouse brain MRI atlas. (B) Two-way mixed-effects model analysis of [^{18}F]UCB-H SUV z-scores of PS19 and C57Bl/6 mice at 5.7, 8.4, 10.0, and 11.0 months of age. Significance levels is BH-FDR-adjusted p value < 0.05 (*).

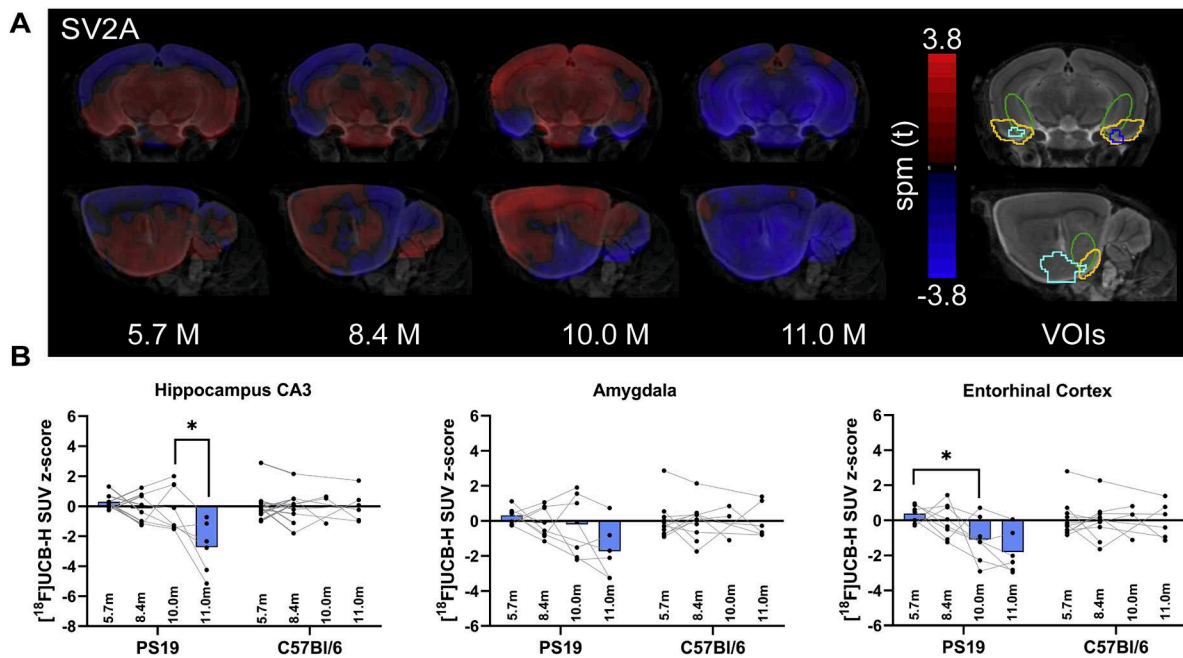


Fig. 3. (A) SPM images show differences in SV2A expression level between PS19 and C57Bl/6 mice in the hippocampus CA3, amygdala, and entorhinal cortex at 5.7, 8.4, 10.0, and 11.0 months of age, with a continuous reduction (depicted in blue) in PS19 mice. The coronal and sagittal planes of target VOIs are projected on a mouse brain MRI atlas. (B) Two-way mixed-effects model analysis of $[^{18}\text{F}]\text{UCB-H}$ SUV z-scores of PS19 and C57Bl/6 mice at 5.7, 8.4, 10.0, and 11.0 months of age. Significance levels is BH-FDR-adjusted p value < 0.05 (*).

BH-FDR correction within the subregions family of tests (Supplemental Fig 1 and Supplemental Table 1).

In PS19 mice, slope analyses across the different time intervals revealed significant overall time effects in the neocortex ($q = 0.001$), hippocampus CA1 ($q = 0.004$), hippocampus CA3 ($q = 0.012$), brainstem ($q = 0.015$), thalamus ($q = 0.004$), hypothalamus ($q = 0.005$) and cerebellum ($q = 0.004$), indicating phased alterations in $[^{18}\text{F}]\text{UCB-H}$ uptake. Among cortical subregions, the piriform cortex ($q = 0.001$), visual cortex ($q = 0.004$), auditory cortex ($q = 0.001$), motor cortex ($q < 0.001$), somatosensory cortex ($q < 0.001$), and olfactory cortex ($q = 0.005$) also showed significant overall time effects, consistent with the phased pattern observed in the neocortex (Table 1). $[^{18}\text{F}]\text{UCB-H}$ PET imaging and adjacent interval slope comparisons suggested a substantial increase trend between 8.4 and 10.0 months of age ($+8.1\% \pm 3.0\%$) in the neocortex ($q = 0.053$), hippocampus CA1 ($q = 0.056$), brainstem ($q = 0.301$), thalamus ($q = 0.053$), hypothalamus ($q = 0.053$), and cerebellum ($q = 0.323$), followed by a rapid decline from 10.0 to 11.0 months of age ($-18.4\% \pm 4.7\%$) (neocortex: $q = 0.053$; hippocampus CA1: $q = 0.053$; brainstem: $q = 0.098$; thalamus: $q = 0.053$; hypothalamus: $q = 0.053$; cerebellum: $q = 0.053$); however, none of these interval-specific changes remained statistically significant after BH-FDR correction. In exploratory cortical subregion analyses, the uptake alteration with an initial increase followed by a decrease was significant in the piriform cortex (both increase and decrease $q = 0.033$) and the somatosensory cortex (both increase and decrease $q = 0.033$). The motor cortex also showed a significant decrease from 10.0 to 11.0 months of age ($q = 0.033$) (Fig. 2A and Supplemental Table 2). In contrast, the hippocampus CA3, amygdala, and entorhinal cortex showed a more continuously decreasing pattern ($-8.8\% \pm 4.8\%$) from 5.7 to 11.0 months of age, but this did not survive BH-FDR correction (Fig. 3A and Supplemental Table 2).

The SV2A expression levels showed a trend toward reduction in PS19 mice compared with C57Bl/6 controls across the primary VOIs at 11.0 months of age ($-8.7\% \pm 3.1\%$). After BH-FDR correction, none of the regional differences reached statistical significance (neocortex: $q = 0.079$; hippocampus CA1: $q = 0.079$; hippocampus CA3: $q = 0.056$; amygdala: $q = 0.077$; brainstem: $q = 0.079$; thalamus: $q = 0.077$;

hypothalamus: $q = 0.079$; cerebellum: $q = 0.146$). In the exploratory cortical subregions, similar decreases in SV2A expression were observed at 11.0 months of age across subregions ($-6.6\% \pm 3.0\%$), though none survived correction (Supplemental Fig 2).

To address potential limitations of SUV in small animal PET, we analyzed the $[^{18}\text{F}]\text{UCB-H}$ PET data using SV2A volume of distribution (V_T) images to normalize for the activity concentration in the blood as an additional tissue-independent normalization approach. Similar patterns of initially elevated and subsequently decreased $[^{18}\text{F}]\text{UCB-H}$ V_T were observed in the neocortex, hippocampus CA1, thalamus, hypothalamus, and cortical subregions. $[^{18}\text{F}]\text{UCB-H}$ V_T persistently decreased in the hippocampus CA3 and amygdala with a noticeable reduction in the entorhinal cortex at 10.0 months of age. These V_T findings were consistent with the SUV results trendwise (Supplemental Fig 3). However, the differences did not reach statistical significance, likely due to the high natural variance of IDIF-based V_T computation.

3.2. The desynchronization index based on $[^{18}\text{F}]\text{UCB-H}$ PET signal shows longitudinal deviation from a reference-derived normative inter-regional SV2A expression pattern in PS19 mice

To allow network level analysis, we calculated the desynchronization index (DI) for the SV2A expression level in PS19 and C57Bl/6 mice at different time points. Therefore we performed the calculations at the hemispheric level. The linear fit obtained from the reference cohort represented the normative inter-regional relationship between each VOI pair. DI is a distance-based and non-directional metric that can only be interpreted as the deviation magnitude of SV2A expression levels in PS19 and C57Bl/6 mice from the reference. After BH-FDR correction, a greater deviation appeared in the left hemisphere, with significant differences between PS19 and C57Bl/6 mice in the left hippocampus CA3 and left motor cortex at 10.0 months of age, as well as in the left visual cortex and left thalamus at 11.0 months of age. In the right hemisphere, significant differences were shown in the entorhinal cortex at both 10.0 and 11.0 months of age. The bilateral amygdala, hypothalamus, and cerebellum exhibited significant differences at 10.0 months of age as well (Table 2). After that, principal component analysis (PCA) was

Table 1

Slopes of [¹⁸F]UCB-H SUV z-scores across the different time intervals in the primary VOIs and exploratory cortical subregions in PS19 mice and overall interval effect.

VOIs	Overall interval effect		Time interval slopes (mean ± SD)		
	(F(df1, df2); q)	η ² ; conditional R ²	Slope 1	Slope 2	Slope 3
Primary					
Neocortex	32.30 (2, 18); 0.001	0.782; 0.755	0.04 ± 0.33	0.87 ± 0.82	-3.03 ± 1.22
Hippocampus CA1	16.36 (2, 18); 0.004	0.645; 0.609	-0.01 ± 0.33	0.63 ± 0.76	-2.11 ± 1.45
Hippocampus CA3	8.38 (2, 18); 0.012	0.482; 0.444	-0.16 ± 0.42	0.01 ± 0.88	-2.23 ± 1.76
Amygdala	1.10 (2, 18); 0.338	0.109; 0.095	-0.15 ± 0.39	-0.14 ± 0.97	-0.88 ± 1.50
Brainstem	6.99 (2, 18); 0.015	0.437; 0.399	-0.12 ± 0.48	0.30 ± 0.73	-1.32 ± 1.15
Thalamus	16.08 (2, 18); 0.004	0.641; 0.605	-0.12 ± 0.37	0.53 ± 0.65	-1.96 ± 1.32
Hypothalamus	12.99 (2, 18); 0.005	0.591; 0.553	-0.18 ± 0.38	0.73 ± 0.76	-1.87 ± 1.53
Cerebellum	9.20 (2, 18); 0.004	0.505; 0.467	-0.11 ± 0.33	0.24 ± 0.63	-1.05 ± 0.63
Exploratory					
Piriform Cortex	24.55(2, 18); 0.001	0.732; 0.700	-0.17 ± 0.36	0.73 ± 0.69	-2.08 ± 1.09
Entorhinal Cortex	0.86(2, 18); 0.403	0.087; 0.076	-0.15 ± 0.45	-0.69 ± 1.05	-0.38 ± 0.94
Visual Cortex	17.61(2, 18); 0.004	0.662; 0.627	0.27 ± 0.44	1.02 ± 1.06	-3.14 ± 2.22
Auditory Cortex	23.78(2, 17); 0.001	0.725; 0.704	0.12 ± 0.27	0.79 ± 0.88	-2.82 ± 1.52
Motor Cortex	29.55(2, 18); <0.001	0.767; 0.738	0.16 ± 0.45	0.80 ± 0.84	-2.52 ± 1.07
Somatosensory Cortex	39.41(2, 18); <0.001	0.814; 0.790	0.14 ± 0.46	1.30 ± 0.97	-3.41 ± 1.42
Olfactory Cortex	12.29(2, 18); 0.005	0.577; 0.539	-0.11 ± 0.36	1.05 ± 1.48	-2.23 ± 1.41

Abbreviations: q, BH-FDR-adjusted p value; η², partial eta-squared; Slope 1-3 refer to the slopes for 5.7-8.4, 8.4-10.0, and 10.0-11.0 months of age, respectively.

performed using the combined data from the above VOIs with significant deviations in SV2A expression to obtain a single read-out for each mouse. We obtained highly differentiated principal component 1 explaining 70.7% of the variance (PC1: F (8, 89) = 19.29, p < 0.0001, η² = 0.634) with strong intergroup discrimination ability. SV2A expression deviation magnitude indicated by PC1 was consistent with SUV z-score findings. Relative to the normative inter-regional pattern, PS19 mice showed the greatest deviation at 10.0 and 11.0 months of age (Ref. vs. 10.0 m PS19: q = 0.001; Ref. vs. 11.0 m PS19: q = 0.004). In PS19 mice, PC1 was significantly larger at 10.0 and 11.0 months of age compared with 5.7 months of age (5.7 vs. 10.0 m: q = 0.004; 5.7 vs. 11.0 m: q = 0.020), and the deviation magnitude at 10.0 months exceeded that at 8.4 months (q = 0.032). However, C57Bl/6 mice showed measurable deviation from the reference at 5.7, 8.4, and 11.0 months as well (all q = 0.004), despite being less pronounced than in PS19 mice. PS19 mice exhibited greater PC1 than C57Bl/6 mice at 10.0 and 11.0 months of age (10.0 m: q = 0.011; 11.0 m: q = 0.038) (Fig. 4 and Supplemental Table 3).

3.3. Significant reduction in SV2A expression and tau accumulation is confirmed by terminal immunohistochemistry in PS19 mice

Terminal immunohistochemical staining was performed for the purpose of PET signal validation and revealed a significant reduction of

Table 2

VOIs with significant desynchronization index differences between PS19 mice and C57Bl/6 controls at 10.0 and 11.0 months of age.

	DI (mean ± SD)		T value	p	q	Cohen's d
	PS19	C57Bl/6				
10.0 months of age						
Hippocampus	4.1 ± 1.1	1.9 ± 0.6	4.032	0.006	0.015	2.250
CA3 LH	2.5 ± 0.5	1.6 ± 0.2	3.859	0.005	0.030	1.857
Amygdala LH	2.2 ± 0.5	1.3 ± 0.2	4.622	0.002	0.027	2.219
Amygdala RH	2.3 ± 0.2	1.6 ± 0.2	5.865	0.004	0.024	3.950
Hypothalamus	3.2 ± 1.0	1.6 ± 0.3	3.785	0.006	0.044	1.786
Cerebellum	5.8 ± 1.4	2.0 ± 0.8	5.459	0.001	0.005	2.965
Entorhinal Cortex RH	3.1 ± 0.9	1.6 ± 0.3	3.769	0.006	0.030	1.784
Motor Cortex LH	2.7 ± 0.5	1.9 ± 0.3	3.029	0.013	0.035	1.749
11.0 months of age						
Thalamus LH	4.4 ± 1.2	2.9 ± 0.8	2.771	0.019	0.047	1.600
Entorhinal Cortex RH	2.6 ± 0.5	1.8 ± 0.3	3.424	0.007	0.034	1.977
Visual Cortex LH						

Cohen's d is reported as PS19 mice minus C57Bl/6 mice (positive values indicate higher DI in PS19 mice). Abbreviations: DI, desynchronization index; p, raw p value; q, BH-FDR-adjusted p value; LH, left hemisphere; RH, right hemisphere.

SV2A in NeuN+ area (%Area) in PS19 mice compared to C57Bl/6 animals (neocortex: q = 0.031, Cohen's d = -2.236; hippocampus CA1: q = 0.012, Cohen's d = -3.448; hippocampus CA3: q = 0.012, Cohen's d = -3.798; brainstem: q = 0.161), confirming the PET results at 11.0 months of age (Fig. 5). The NeuN staining for mature neurons showed a lower signal in PS19 mice than C57Bl/6 controls in the amygdala (q = 0.020, Cohen's d = -3.087) and thalamus (q = 0.008, Cohen's d = -3.980). However, there were no significant group differences in other cortical regions, limbic system regions, brainstem, and cerebellum (Supplemental Fig 4). AT8 coverage (%Area) was significantly higher in the hippocampus CA3 (q = 0.016, Cohen's d = 6.586) of PS19 mice than in C57Bl/6 mice. Furthermore, the tau accumulation as assessed by AT8 showed a trend towards negative correlation with the SV2A-PET results in the primary regions and cortical subregions at 11.0 months of age. However, these associations were not statistically significant and should be interpreted cautiously due to the small sample size (n = 4) (Fig. 6 and Supplemental Fig 5).

3.4. Longitudinal [¹⁸F]UCB-H PET signal variation shows a negative association with early activated microglia and a disturbed association with reactive astrogliosis in PS19 mice compared to wild-type mice

The area under the curve (AUC) of [¹⁸F]UCB-H SUV z-scores from 8.4 to 11.0 months of age was calculated to reflect the SV2A expression level alterations. To assess if [¹⁸F]GE-180 as marker for activated microglia or [¹⁸F]F-DED as marker for reactive astrogliosis might display any predictive value, we performed a Pearson's correlation for both neuro-inflammation biomarkers. In PS19 mice, a negative association was observed between [¹⁸F]GE-180 SUV z-score and [¹⁸F]UCB-H AUC in the hypothalamus (R = -0.839, p = 0.037) and piriform cortex (R = -0.879, p = 0.021). Conversely, the positive associations were observed in the neocortex (R = 0.887, p = 0.018), amygdala (R = 0.841, p = 0.036), and cerebellum (R = 0.842, p = 0.036), as well as in cortical subregions including the piriform cortex (R = 0.822, p = 0.045), entorhinal cortex (R = 0.813, p = 0.049), visual cortex (R = 0.886, p = 0.019), auditory cortex (R = 0.817, p = 0.047), motor cortex (R = 0.815, p = 0.048), and somatosensory cortex (R = 0.918, p = 0.010) in C57Bl/6 mice.

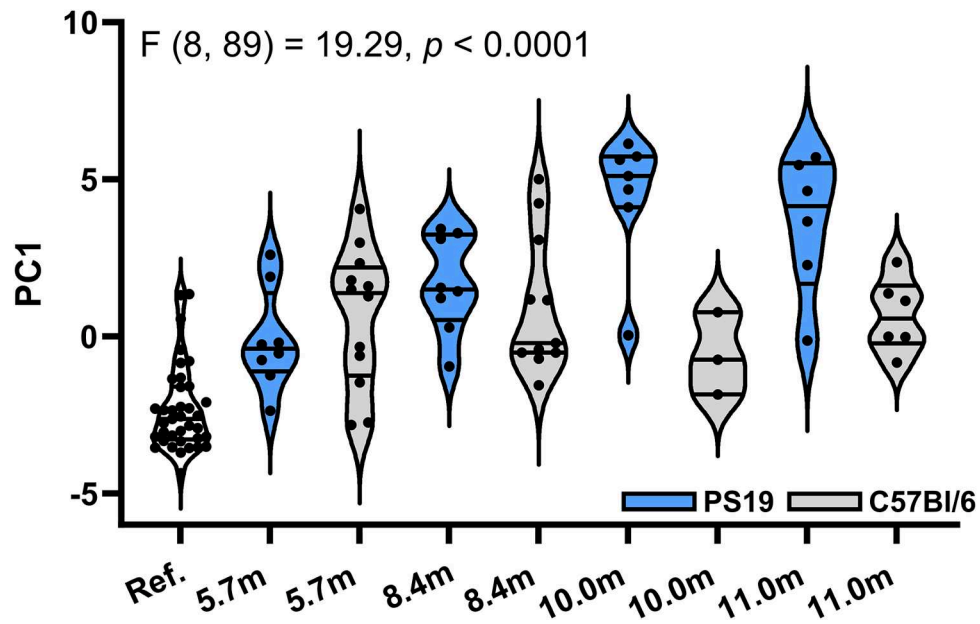


Fig. 4. First principal component (PC1) derives from the VOIs with significant differences in DI. The p value of one-way ANOVA is shown on top. Abbreviations: Ref., reference cohort.

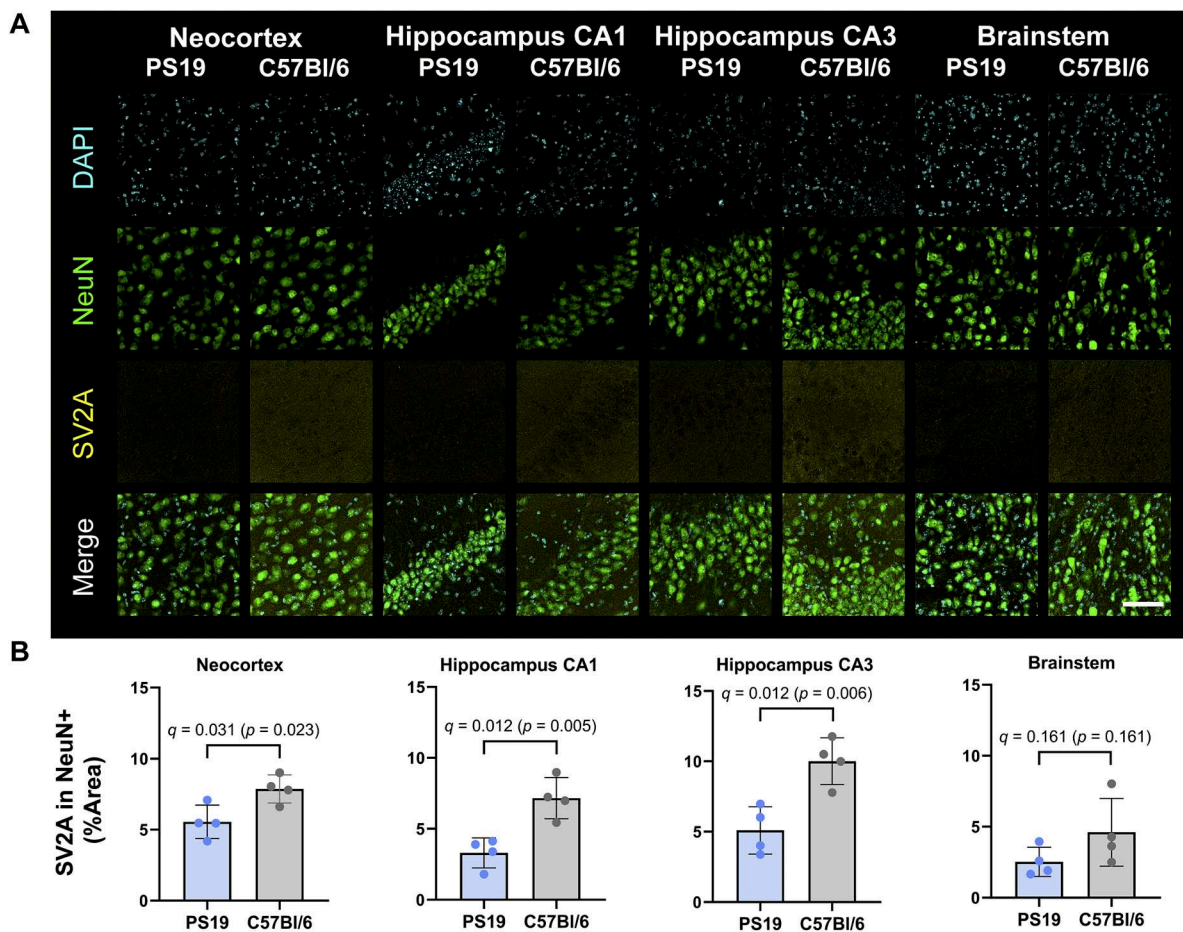


Fig. 5. Representative maximum projections of immunohistochemical stainings in the neocortex, hippocampus CA1 and CA3, and the brainstem together with immunohistochemical analysis of SV2A expression level in the respective regions of PS19 mice and C57Bl/6 controls. q denotes p-values after correction, whereas p denotes raw p-values. Scale bar = 50 μ m.

However, none of the correlations remained significant after BH-FDR correction (Fig. 7A and Supplemental Table 4).

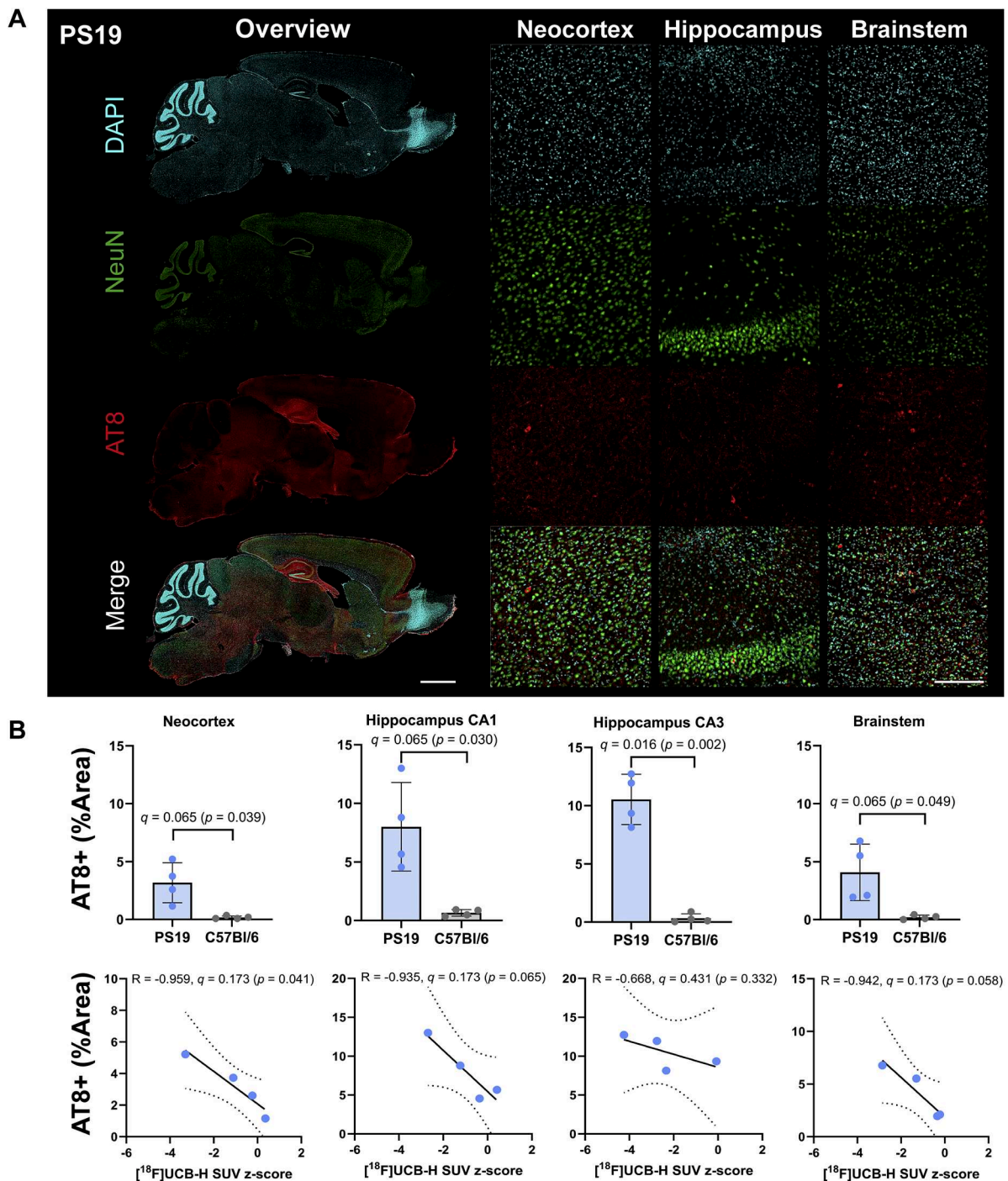


Fig. 6. Representative maximum projections of immunohistochemical stainings for the overview images (scale bar = 1500 μm) and high-magnification images (scale bar = 200 μm) of mature neurons and tau accumulation together with immunohistochemical analysis in PS19 mice, and the correlation between $[^{18}\text{F}]\text{UCB-H}$ uptake and tau accumulation in PS19 mice at 11.0 months of age. q denotes p -values after correction, whereas p denotes raw p -values.

A significant positive correlation between $[^{18}\text{F}]\text{F-DED}$ SUV z-score and $[^{18}\text{F}]\text{UCB-H}$ AUC was shown in the brainstem ($R = 0.949$, $q = 0.032$) in C57Bl/6 mice. Additionally, the positive association was observed in the thalamus ($R = 0.895$, $p = 0.016$) and piriform cortex ($R = 0.878$, $p = 0.021$) in C57Bl/6 mice; however, these associations did not survive BH-FDR correction (both $q > 0.05$). In PS19 mice, the correlations across the primary regions and cortical subregions were mostly weak and varied widely ($R = -0.246$ to 0.733), and none were significant either before or after BH-FDR correction (Fig. 7B and Supplemental Table 5).

4. Discussion

In this study, we performed multi-tracer PET imaging to assess longitudinal SV2A expression changes in a tauopathy mouse model and investigated the association of SV2A expression levels, terminal tau accumulation, and early neuroinflammation. Our key findings are: (1) SV2A expression levels in selected regions change in a phased manner rather than along a linear trajectory in PS19 mice, together with greater deviation from the reference-derived normative inter-regional pattern than in C57Bl/6 mice. (2) The terminal 4R tau pathology is profound and shows a trend towards a negative association with SV2A expression

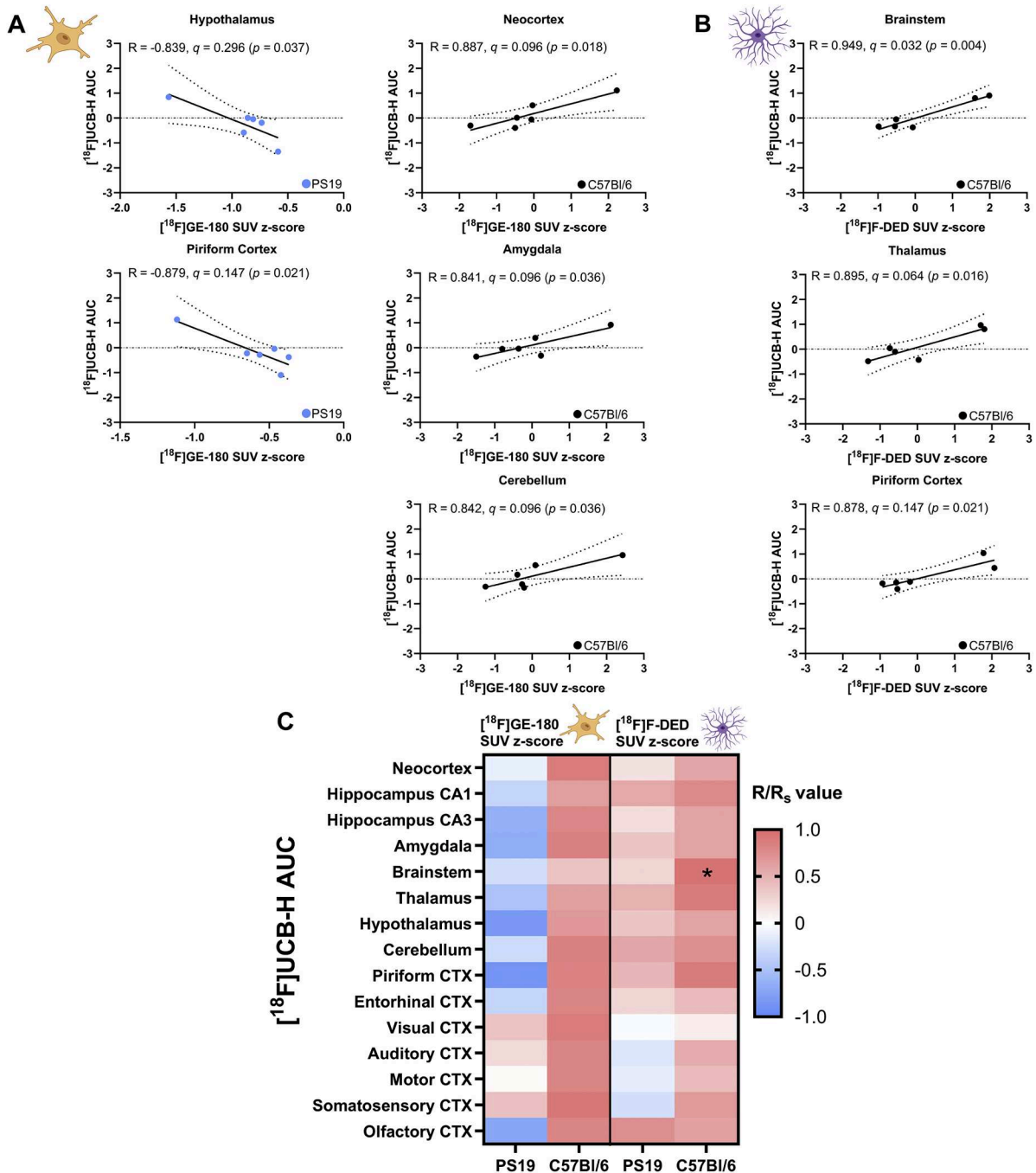


Fig. 7. (A, B) Correlation of SV2A expression level variation (AUC) from 8.4 to 11.0 months with baseline [¹⁸F]GE-180 and [¹⁸F]F-DED uptake. (C) The overview of the correlation between [¹⁸F]UCB-H AUC and baseline [¹⁸F]F-DED and [¹⁸F]GE-180 uptake across the primary VOIs and exploratory cortical subregions by heatmap with separated data from PS19 and C57Bl/6 mice. *q* denotes *p*-values after correction, whereas *p* denotes raw *p*-values. Significance levels are *q* < 0.05 (*). Abbreviations: AUC, area under the curve.

level loss in PS19 mice. (3) Exploratory correlation analyses suggest that the associations between longitudinal variations in SV2A expression levels and early neuroinflammation differ between PS19 and C57Bl/6 mice.

The significant genotype × time interactions remained in the neocortex and hippocampus CA3 after BH-FDR correction, indicating that longitudinal trajectories indeed differed between PS19 and C57Bl/6 mice. *V_T* image analysis results verified the main SUV-derived findings for [¹⁸F]UCB-H in the corresponding regions. Building upon this, we analyzed time interval slopes to characterize non-linear temporal trajectories and the time windows of SV2A-PET uptake changes in PS19

mice. The PS19 mice exhibited a sustained decrease in SV2A expression levels in the hippocampus CA3, amygdala, and entorhinal cortex. The global reduction trend in SV2A-PET uptake was shown in PS19 mice at 11.0 months of age, consistent with the severe and widespread synaptic loss reported in AD, PSP, and CBD patients (Mecca et al., 2020, Holland et al., 2020, Bastin et al., 2020). However, compared with the age-matched C57Bl/6 controls, the PS19 mice had an upward trend in SV2A expression level between 8.4 and 10.0 months of age, followed by a rapid decline from 10.0 to 11.0 months of age in the neocortex, hippocampus CA1, brainstem, thalamus, hypothalamus, and cerebellum. This biphasic pattern of change reached statistical significance in the

piriform cortex and somatosensory cortex. Given the limited sample size in the present study, repeating equivalent slope tests in the C57Bl/6 mice would increase the burden of multiple comparisons while providing limited benefit in explaining disease-related trajectory differences; therefore, it was not prioritized.

To our knowledge, this study is the first to report elevated SV2A expression levels in multiple brain regions in a mouse model of pure tau pathology using SV2A-PET imaging. However, this finding contrasts with most reports describing reduced SV2A expression levels in patients with NDDs (Wang et al., 2024, Mecca et al., 2020, Bastin et al., 2020, Chen et al., 2018, Coomans et al., 2021). We initially considered that this divergence might be attributable to the long disease duration in clinical cohorts, coupled with imaging being conducted at relatively advanced stages, such that a transient early increase in SV2A expression could be missed. However, available evidence has suggested that healthy aging does not lead to significant changes in SV2A expression levels (Michiels et al., 2021), and patients with amnesic mild cognitive impairment, an early state of dementia, have still shown significantly reduced SV2A-PET signals in the temporal lobe and hippocampus (Chen et al., 2018, O'Dell et al., 2021, Vanderlinden et al., 2022). Only isolated cases have reported focal increases in SV2A binding (Chen et al., 2018). A recent study further suggested that longitudinal SV2A expression levels may show a positive association with cortical tau burden, yet definitive evidence of increased SV2A expression remains lacking (Wang et al., 2025). One possible explanation for the transient and phased increase in SV2A-PET signals observed here is neuronal hyperexcitability. This possibility is biologically plausible because neuronal hyperexcitability has been linked to tau progression and cognitive decline (Wilson et al., 2023, Robbins et al., 2021), and synaptic vesicle proteins may participate in activity-dependent tau release (Tracy et al., 2022). Notably, a similar rise in SV2A expression has also been detected in a model of pure A β pathology (APPSL70), although the peak signal of SV2A-PET occurred later than in PS19 mice (11.0 vs 10.0 months) (Kunze et al., 2025). This is potentially due to a longer latency period between A β deposition and the onset of neurodegeneration, or a tighter spatiotemporal coupling between tau aggregation and synaptic activity (Vanderlinden et al., 2022, Jack et al., 2013, Jansen et al., 2015, Groot et al., 2024). It should be emphasized that SV2A-PET reflects synaptic vesicle protein levels rather than directly measuring neuronal activity or function. Moreover, we lack direct evidence for transient increases in SV2A during disease progression, as well as electrophysiological data; therefore, the interpretation above should be regarded as speculative.

In this study, the DI is a non-directional distance metric derived from linear relationships between VOI pairs in the reference cohort, quantifying the magnitude of deviation in SV2A expression levels from the normative inter-regional pattern established in reference cohort (Zatcepin et al., 2024). It therefore provides no directional information, cannot distinguish strengthening, weakening, or reorganization of inter-regional relationships, and is limited in capturing potential non-linear inter-regional network interactions. Alterations in SV2A expression levels are region-selective and stage-dependent (Vanderlinden et al., 2022, Luan et al., 2025); thus, such deviations do not emerge synchronously across all brain regions. Accordingly, after identifying VOIs with significant DI differences, we restricted the PCA input to affected regions to reduce noise introduced by unaffected regions and to avoid dilution or masking of disease-related deviation signals. We acknowledge that this thresholding may introduce selection bias and potential circularity. Accordingly, PC1 is presented only as a descriptive summary of deviation in affected regions at corresponding time points. Future studies with larger cohorts should assess robustness and generalizability by predefining VOI sets, sensitivity analyses, cross-validation, and unsupervised PCA across all VOIs.

We observed measurable deviations in the inter-regional uptake patterns of C57Bl/6 mice relative to the reference, which may reflect physiological variation or individual differences during normal ageing. However, PS19 mice showed a greater deviation magnitude from the

reference, most pronounced at 10.0 and 11.0 months of age, exceeding that observed in age-matched C57Bl/6 controls. In parallel, longitudinal multi-timepoint, multi-region SV2A-PET analyses suggested a potential spatiotemporal mismatch in SV2A expression in PS19 mice. It should be noted that the non-linear evidence in this study arises primarily from the temporal dimension (phased alterations in uptake), whereas quantification of inter-regional relationships is still based on a linear model. We did not directly measure spatiotemporal synchronization or connectivity, and we lack independent validation that DI corresponds to genuine network dysfunction. Whether this deviation or mismatch relates to specific functional disturbances remains unclear, however, we speculate that this deviation or mismatch may relate to neuronal hyperexcitability, potentially involving more complex network disruptions. Consequently, we strictly interpret DI and PC1 as indices of deviation magnitude, and we use desynchronization index solely as a label for this quantitative measure. Future integration of functional MRI (e.g., time-resolved connectivity) (Panda et al., 2022), electrophysiological recordings, and spatiotemporal dynamical modeling would help clarify the biological meaning of DI.

SV2A expression levels were significantly reduced in PS19 mice at 11.0 months of age, as assessed by immunohistochemical staining. Moreover, these mice showed profound tau accumulation in the hippocampus CA3, and the tau pathology burden showed a strong but non-significant negative association with SV2A expression levels across most brain regions, suggesting progressive disease involvement. However, this association was weaker in other regions, particularly in the amygdala, hypothalamus, and somatosensory cortex. This attenuated association likely reflects the spatiotemporal progression of tau pathology. In PS19 mice, tau pathology originates in the entorhinal cortex and progresses rostrally, involving the piriform cortex early in disease progression, and subsequently advances to the hippocampus and amygdala, with continued accumulation in the limbic system, thalamus, and hypothalamus. At later stages, tau pathology extends to deep neocortical layers and subcortical nuclei, accompanied by neurodegenerative changes (Hurtado et al., 2010). Accordingly, region-specific stage differences in tau burden may contribute to a heterogeneous association between tau and SV2A expression levels. In addition, given the small sample size, these correlation estimates are likely unstable and sensitive to individual data points and should be interpreted cautiously.

Most studies investigating the relationship between tau accumulation and SV2A expression levels in AD primarily focus on clinical patients rather than rodent models. This is mainly because commonly used preclinical models, amyloid precursor protein (APP) transgenic mice (e.g., APP/PS1, Tg-ArcSwe, APPNL-GF), do not reliably recapitulate the proportional 3R/4R tau pathology observed in humans (Yokoyama et al., 2022). Although a PS19 \times PDAPP double transgenic mouse model has been developed and shows a tau spreading pattern similar to that in PS19 mice, tau pathology remains predominantly 4R (Hurtado et al., 2010). To date, mouse models expressing endogenous 3R/4R tau proteins can be generated via stereotactic injection or genome editing (Hosokawa et al., 2022); however, these models have not yet been used to assess differences in SV2A expression. The clinical studies revealed a negative correlation between baseline tau burden and SV2A-PET uptake across the entire cortex among AD patients (Coomans et al., 2021, Wang et al., 2025). An additional study demonstrated a negative association between tau accumulation in the entorhinal cortex and SV2A-PET uptake in the hippocampus of AD patients, suggesting that tau pathology arising from entorhinal neurons may contribute to synaptic loss in hippocampal neurons receiving projections from this region (Mecca et al., 2022). Other research suggested the synaptic loss pattern was also associated with brain network connectivity (Luan et al., 2025). Overall, the direct relationship between regional tau accumulation and the propagation of synaptic loss remains unclear. Given the substantial heterogeneity of tauopathies, SV2A expression levels and alteration patterns may differ across distinct tau pathological contexts (4R tau, 3R/4R tau, or 3R tau). Therefore, there is an urgent need to develop and

compare animal models that more accurately reflect the underlying mechanisms of the disease.

Quantitative analysis of neuronal staining revealed no significant differences in most regions between PS19 and C57Bl/6 mice despite a reduction in SV2A expression level, suggesting that synaptic loss and degeneration typically precede neuronal loss and that the resulting neural network dysfunction is an early event contributing to disease progression (Selkoe, 2002, Palop and Mucke, 2010, Henstridge et al., 2016, Palop and Mucke, 2016).

We found a non-significant negative association between SV2A expression variation and the 18 kDa translocator protein (TSPO) expression, which is upregulated in activated microglia (Eckenweber et al., 2020), in the hypothalamus and piriform cortex. Therefore, we speculated that early microglia-related inflammatory signals may show a region-specific association with longitudinal SV2A expression level changes. Previous studies reported that microglial activation can promote pathological propagation and is related to neurotoxicity (Spangenberg et al., 2016, Leyns et al., 2017, Pascoal et al., 2021, Wang et al., 2022), and may contribute to neuronal circuit remodeling by affecting synaptic homeostasis and sustained inflammatory signaling (Dejanovic et al., 2022, Chen et al., 2025, Chia et al., 2025, Hansen et al., 2018). We previously observed in APPSL70 mice that microglial activation propagated jointly with increasing SV2A expression, more closely than reactive astrogliosis did, which may indirectly reflect an association between activated microglia and excitotoxicity (Kunze et al., 2025). However, an opposite correlation pattern was observed in C57Bl/6 mice. Existing evidence indicates that microglia possess both inflammatory immune functions and non-inflammatory housekeeping roles, and that the microglial activation subtypes show disease stage-specific characteristics (Hansen et al., 2018, Hamelin et al., 2016, Deczkowska et al., 2020, Kim et al., 2022). On this basis, the TSPO activity detected in the early-stage PS19 mice may reflect heterogeneous microglial responses rather than a single disease-related mechanism. It should be emphasized that these interpretations are primarily based on correlational observations and prior literature, and currently lack direct experimental validation.

SV2A expression variation was significantly positively correlated with baseline monoamine oxidase (MAO-B) activity, a marker of reactive astrogliosis (Ballweg et al., 2023), in the brainstem. However, this correlation was primarily contributed by C57Bl/6 mice, with no significant associations observed across brain regions in PS19 mice. These findings suggest that early astrocytic activation may be more closely linked to healthy aging than to the disease state. Astrocytes are a crucial component of the tripartite synaptic network, involved in maintaining glutamate homeostasis and modulating synaptic transmission (Liu et al., 2021). However, early dysfunction of astrocyte support may also occur in disease states. The extensive research indicates that reactive astrogliosis could lead to impaired neurotransmitter clearance and dysregulated Ca^{2+} (Piacentini et al., 2017), thereby triggering excitotoxicity (Song et al., 2018, Gamba et al., 2021, Quincozes-Santos et al., 2021, Brandebura et al., 2023) and disrupting synaptic homeostasis (Starenghi et al., 2021, Bhalla et al., 2025). Therefore, although our results did not identify a correlation between reactive astrogliosis and SV2A expression levels in PS19 mice, and the current evidence is insufficient for mechanistic inference, the potential role of reactive astrogliosis in driving disease progression warrants further investigation.

This study has additional limitations. First, voxel-wise SPM analyses were displayed at an uncorrected voxel-level $p < 0.05$ without multiple-comparison correction and should therefore be interpreted as exploratory. Second, the sample size in this study was relatively modest (PS19: $n = 8$; C57Bl/6: $n = 12$), but is comparable to that commonly used in prior preclinical PET studies (Takkinen et al., 2018, Endepols et al., 2024). Not all animals contributed usable data at every follow-up time point, which reduced the effective sample size at certain time points ($n = 4$ or 6), thereby decreasing statistical power and increasing estimation

uncertainty. Although several correlation analyses yielded high correlation coefficients, such estimates are unstable and highly sensitive to single data points in small samples. Furthermore, SUV may be influenced by peripheral metabolism, clearance, and tracer delivery in small animal PET studies. However, our key findings were trendwise confirmed by V_T , which has been described as a more unbiased approach (Vogler et al., 2023), across major brain regions. Nevertheless, peripheral confounding effects on SUV-derived measures cannot be fully excluded. Finally, to further investigate the biological basis of the observed increase in SV2A expression levels, additional electrophysiological studies would be valuable, such as multi-electrode array recordings, electroencephalography, and Ca^{2+} imaging at corresponding time points of elevated SV2A expression. We recorded baseline TSPO and MAO-B activity to explore whether early activated gliosis is associated with longitudinal SV2A expression changes and may also have predictive value. In this context, conducting further longitudinal multi-tracer imaging scans at matched time points or depletion experiments of microglia and astrocytes would hold great research value. In summary, the interplay among pathology, SV2A-related synaptic alterations, and glial activation states reflects a complex and dynamic regulatory network that requires a deeper exploration of the spatio-temporal relationships among them.

5. Conclusion

In this multimodal imaging study, [^{18}F]UCB-H PET reflected phased, non-linear changes in SV2A expression levels during pathology progression in an animal model of 4R tauopathy, characterized by an increase followed by a rapid decrease in selected regions. Meanwhile, PS19 mice exhibited a significantly greater deviation from the reference-derived normative inter-regional pattern of SV2A expression levels than C57Bl/6 mice.

Late-stage 4R tau deposition was profound and tended to show a negative association with the loss of SV2A expression levels detected by [^{18}F]UCB-H PET in PS19 mice.

Associations of longitudinal SV2A expression variation with TSPO and MAO-B PET measures differed between PS19 and wild-type mice, with negative trends observed for activated microglia in selected regions and disturbed associations with reactive astrogliosis in PS19 mice. We thus speculate that the observed increase and deviation magnitude in SV2A expression levels may potentially reflect neuronal hyperexcitability preceding neurodegeneration, and early microglial-driven pruning and astrocytic dysfunction in vulnerable regions may contribute to these changes, but causality cannot be inferred.

Concluding, [^{18}F]UCB-H PET provides a feasible approach to monitor the dynamic changes of SV2A expression levels in the mouse model of primary tauopathy, and inter-regional deviation metrics may provide an indirect marker of regional synaptic alterations.

Glossary

AD, Alzheimer's disease; A β , β -amyloid; APP, amyloid precursor protein; AUC, area under the curve; CBD, corticobasal degeneration; DI, desynchronization index; FTD, frontotemporal dementia; BH-FDR, Benjamini-Hochberg false discovery rate; partial eta-squared, η^2 ; IDIF, image-derived input function; MAO-B, monoamine oxidase; NDDs, neurodegenerative diseases; NFTs, neurofibrillary tangles; PSP, progressive supranuclear palsy; PET, positron emission tomography; PCA, principal component analysis; PC1, first principal component; SV2A, synaptic vesicle protein 2A; SUV, standardized uptake value; SPM, statistical parametric mapping; TSPO, translocator protein; VOI, volume of interest; V_T , volume-of-distribution.

Funding

This research did not receive any specific grant from funding

agencies in the public, commercial, or not-for-profit sectors.

Declaration of generative AI and AI-assisted technologies in the manuscript preparation process

During the preparation of this work, the author used OpenAI GPT-4o mini in order to improve language and readability. After using this tool, the author reviewed and edited the content as needed and take full responsibility for the content of the published article.

Data availability statement

PET images, immunohistochemical images, and datasets generated and analyzed during this study are available from the corresponding author on reasonable request.

CRediT authorship contribution statement

Yunlei Li: Writing – original draft, Visualization, Validation, Software, Resources, Methodology, Investigation, Formal analysis, Data curation, Conceptualization. **Artem Zatcepin:** Software, Resources, Methodology. **Giovanna Palumbo:** Investigation. **Rosel Oos:** Investigation. **Karin Wind-Mark:** Project administration, Investigation. **Simon Lindner:** Resources, Project administration. **Franz-Josef Gildehaus:** Resources, Methodology. **Johannes Gnörich:** Software, Resources, Methodology. **Rudolf A Werner:** Writing – review & editing, Supervision, Project administration. **Matthias Brendel:** Writing – review & editing, Visualization, Supervision, Software, Resources, Project administration, Methodology, Funding acquisition, Formal analysis, Conceptualization. **Lea H Kunze:** Writing – review & editing, Visualization, Validation, Software, Resources, Project administration, Methodology, Investigation, Formal analysis, Data curation, Conceptualization.

Declaration of competing interest

MB is a member of the Neuroimaging Committee of the EANM. MB has received speaker honoraria from Roche, GE Healthcare, and Life Molecular Imaging and serves as an advisor of MIAC and Life Molecular Imaging. RAW has received speaker honoraria from Novartis/AAA and PentixaPharm and reports advisory board work for Novartis/AAA and Bayer. No other potential competing interest relevant to this study exists.

Acknowledgements

We would like to thank Dr. Lothar Lindemann and the Hoffmann La-Roche AG for providing the mice and the funding for the reference cohort used to determine the desynchronization index.

Supplementary materials

Supplementary material associated with this article can be found, in the online version, at [doi:10.1016/j.neuroimage.2026.121932](https://doi.org/10.1016/j.neuroimage.2026.121932).

References

- Bajjalieh, S.M., Peterson, K., Shinghal, R., Scheller, R.H., 1992. SV2, a brain synaptic vesicle protein homologous to bacterial transporters. *Science* (1979) 257, 1271–1273. <https://doi.org/10.1126/science.1519064>.
- Ballweg, A., et al., 2023. [18F]F-DED PET imaging of reactive astrogliosis in neurodegenerative diseases: preclinical proof of concept and first-in-human data. *J. Neuroinflammation*. 20, 68. <https://doi.org/10.1186/s12974-023-02749-2>.
- Bastin, C., et al., 2020. In vivo imaging of synaptic loss in Alzheimer's disease with [18F]UCB-H positron emission tomography. *Eur. J. Nucl. Med. Mol. Imaging* 47, 390–402. <https://doi.org/10.1007/s00259-019-04461-x>.

- Bhalla, M., et al., 2025. SIRT2 and ALDH1A1 as critical enzymes for astrocytic GABA production in Alzheimer's disease. *Mol. Neurodegener.* 20, 6. <https://doi.org/10.1186/s13024-024-00788-8>.
- Brandebura, A.N., Paumier, A., Onur, T.S., Allen, N.J., 2023. Astrocyte contribution to dysfunction, risk and progression in neurodegenerative disorders. *Nature Rev. Neurosci.* 24, 23–39. <https://doi.org/10.1038/s41583-022-00641-1>.
- Brendel, M., et al., 2016. Glial activation and glucose metabolism in a transgenic amyloid mouse model: a triple-tracer PET study. *J. Nucl. Med.* 57, 954–960. <https://doi.org/10.2967/jnumed.115.167858>.
- Brendel, M., et al., 2016. Small-animal PET imaging of tau pathology with 18F-THK5117 in 2 transgenic mouse models. *J. Nucl. Med.* 57, 792–798. <https://doi.org/10.2967/jnumed.115.163493>.
- Buchholz, S., et al., 2025. The tau isoform 1N4R confers vulnerability of MAPT knockout human iPSC-derived neurons to amyloid beta and phosphorylated tau-induced neuronal dysfunction. *Alzheimers. Dement.* 21, e14403. <https://doi.org/10.1002/alz.14403>.
- Chen, M.K., et al., 2018. Assessing synaptic density in Alzheimer disease with synaptic vesicle glycoprotein 2A positron emission tomographic imaging. *JAMA Neurol.* 75, 1215–1224. <https://doi.org/10.1001/jamaneurol.2018.1836>.
- Chen, Z.P., et al., 2025. GABA-dependent microglial elimination of inhibitory synapses underlies neuronal hyperexcitability in epilepsy. *Nat. Neurosci.* 28, 1404–1417. <https://doi.org/10.1038/s41593-025-01979-2>.
- Chia, S.Y., et al., 2025. Single-nucleus transcriptomics reveals a distinct microglial state and increased MSRI-mediated phagocytosis as common features across dementia subtypes. *Genome Med.* 17, 92. <https://doi.org/10.1186/s13073-025-01519-4>.
- Chung, D.C., Roemer, S., Petrucelli, L., Dickson, D.W., 2021. Cellular and pathological heterogeneity of primary tauopathies. *Mol. Neurodegener.* 16, 57. <https://doi.org/10.1186/s13024-021-00476-x>.
- Coomans, E.M., et al., 2021. In vivo tau pathology is associated with synaptic loss and altered synaptic function. *Alzheimers. Res. Ther.* 13, 35. <https://doi.org/10.1186/s13195-021-00772-0>.
- Deczkowska, A., Weiner, A., Amit, I., 2020. The physiology, pathology, and potential therapeutic applications of the TREM2 signaling pathway. *Cell* 181, 1207–1217. <https://doi.org/10.1016/j.cell.2020.05.003>.
- Dejanovic, B., et al., 2022. Complement C1q-dependent excitatory and inhibitory synapse elimination by astrocytes and microglia in Alzheimer's disease mouse models. *Nat. Aging* 2, 837–850. <https://doi.org/10.1038/s43587-022-00281-1>.
- Eckenweber, F., et al., 2020. Longitudinal TSP0 expression in tau transgenic P301S mice predicts increased tau accumulation and deteriorated spatial learning. *J. Neuroinflammation*. 17, 208. <https://doi.org/10.1186/s12974-020-01883-5>.
- Endepols, H., et al., 2024. Fragmentation of functional resting state brain networks in a transgenic mouse model of tau pathology: a metabolic connectivity study using [18F]FDG-PET. *Exp. Neurol.* 372, 114632. <https://doi.org/10.1016/j.expneurol.2023.114632>.
- Finnema, S.J., et al., 2016. Imaging synaptic density in the living human brain. *Sci. Transl. Med.* 8, 348ra396. <https://doi.org/10.1126/scitranslmed.aaf6667>.
- Gamba, P., et al., 2021. The controversial role of 24-S-hydroxycholesterol in Alzheimer's Disease. *Antioxidants (Basel)* 10, 740. <https://doi.org/10.3390/antiox10050740>.
- Gnörich, J., et al., 2023. Depletion and activation of microglia impact metabolic connectivity of the mouse brain. *J. Neuroinflamm.* 20, 47. <https://doi.org/10.1186/s12974-023-02735-8>.
- Groot, C., et al., 2024. Tau positron emission tomography for predicting dementia in individuals with mild cognitive impairment. *JAMA Neurol.* 81, 845–856. <https://doi.org/10.1001/jamaneurol.2024.1612>.
- Hamelin, L., et al., 2016. Early and protective microglial activation in Alzheimer's disease: a prospective study using 18F-DPA-714 PET imaging. *Brain* 139, 1252–1264. <https://doi.org/10.1093/brain/aww017>.
- Han, T., Xu, Y., Sun, L., Hashimoto, M., Wei, J., 2024. Microglial response to aging and neuroinflammation in the development of neurodegenerative diseases. *Neural Regen. Res.* 19, 1241–1248. <https://doi.org/10.4103/1673-5374.385845>.
- Hansen, D.V., Hanson, J.E., Sheng, M., 2018. Microglia in Alzheimer's disease. *J. Cell Biol.* 217, 459–472. <https://doi.org/10.1083/jcb.201709069>.
- Heneka, M.T., et al., 2024. Neuroinflammation in Alzheimer disease. *Nat. Rev. Immunol.* 25, 321–352. <https://doi.org/10.1038/s41577-024-01104-7>.
- Henstridge, C.M., Pickett, E., Spiers-Jones, T.L., 2016. Synaptic pathology: a shared mechanism in neurological disease. *Ageing Res. Rev.* 28, 72–84. <https://doi.org/10.1016/j.arr.2016.04.005>.
- Hickman, S., Izzy, S., Sen, P., Morsett, L., El Khoury, J., 2018. Microglia in neurodegeneration. *Nat. Neurosci.* 21, 1359–1369. <https://doi.org/10.1038/s41593-018-0242-x>.
- Holland, N., et al., 2020. Synaptic loss in primary tauopathies revealed by [11C]UCB-J positron emission tomography. *Mov. Disord.* 35, 1834–1842. <https://doi.org/10.1002/mds.28188>.
- Hong, S., et al., 2016. Complement and microglia mediate early synapse loss in Alzheimer mouse models. *Science* (1979) 352, 712–716. <https://doi.org/10.1126/science.aad8373>.
- Hosokawa, M., et al., 2022. Development of a novel tau propagation mouse model endogenously expressing 3 and 4 repeat tau isoforms. *Brain* 145, 349–361. <https://doi.org/10.1093/brain/awab289>.
- Hurtado, D.E., et al., 2010. Abeta accelerates the spatiotemporal progression of tau pathology and augments tau amyloidosis in an Alzheimer mouse model. *Am. J. Pathol.* 177, 1977–1988. <https://doi.org/10.2353/ajpath.2010.100346>.
- Jack Jr., C.R., et al., 2013. Tracking pathophysiological processes in Alzheimer's disease: an updated hypothetical model of dynamic biomarkers. *Lancet Neurol.* 12, 207–216. [https://doi.org/10.1016/S1474-4422\(12\)70291-0](https://doi.org/10.1016/S1474-4422(12)70291-0).

- Jack Jr., C.R., et al., 2018. NIA-AA research framework: toward a biological definition of Alzheimer's disease. *Alzheimer's Dementia* 14, 535–562. <https://doi.org/10.1016/j.jalz.2018.02.018>.
- Jansen, W.J., et al., 2015. Prevalence of cerebral amyloid pathology in persons without dementia. *JAMA* 313, 1924. <https://doi.org/10.1001/jama.2015.4668>.
- Jha, M.K., et al., 2018. Functional dissection of astrocyte-secreted proteins: implications in brain health and diseases. *Prog. Neurobiol.* 162, 37–69. <https://doi.org/10.1016/j.pneurobio.2017.12.003>.
- Kim, D.W., et al., 2022. Amyloid-beta and tau pathologies act synergistically to induce novel disease stage-specific microglia subtypes. *Mol. Neurodegener.* 17, 83. <https://doi.org/10.1186/s13024-022-00589-x>.
- Kunze, L.H., et al., 2025. Fibrillar amyloidosis and synaptic vesicle protein expression progress jointly in the cortex of a mouse model with beta-amyloid pathology. *Neuroimage* 310, 121165. <https://doi.org/10.1016/j.neuroimage.2025.121165>.
- Kwon, S.E., Chapman, E.R., 2012. Glycosylation is dispensable for sorting of synaptotagmin 1 but is critical for targeting of SV2 and synaptophysin to recycling synaptic vesicles. *J. Biol. Chem.* 287, 35658–35668. <https://doi.org/10.1074/jbc.M112.398883>.
- Leyns, C.E.G., et al., 2017. TREM2 deficiency attenuates neuroinflammation and protects against neurodegeneration in a mouse model of tauopathy. *Proc. Natl. Acad. Sci. U S A* 114, 11524–11529. <https://doi.org/10.1073/pnas.1710311114>.
- Liu, X., et al., 2021. Astrocytes in neural circuits: key factors in synaptic regulation and potential targets for neurodevelopmental disorders. *Front. Mol. Neurosci.* 14, 729273. <https://doi.org/10.3389/fnmol.2021.729273>.
- Logan, J., et al., 1990. Graphical analysis of reversible radioligand binding from time-activity measurements applied to [N-11C-Methyl]-(-)-Cocaine PET studies in human subjects. *J. Cerebral Blood Flow Metabol.* 10, 740–747. <https://doi.org/10.1038/jcbfm.1990.127>.
- Luan, Y., et al., 2025. Synaptic loss pattern is constrained by brain connectome and modulated by phosphorylated tau in Alzheimer's disease. *Nat. Commun.* 16, 6356. <https://doi.org/10.1038/s41467-025-61497-4>.
- Ma, Y., et al., 2005. A three-dimensional digital atlas database of the adult C57BL/6J mouse brain by magnetic resonance microscopy. *Neuroscience* 135, 1203–1215. <https://doi.org/10.1016/j.neuroscience.2005.07.014>.
- Mecca, A.P., et al., 2020. In vivo measurement of widespread synaptic loss in Alzheimer's disease with SV2A PET. *Alzheimer's Dementia* 16, 974–982. <https://doi.org/10.1002/alz.12097>.
- Mecca, A.P., et al., 2022. Synaptic density and cognitive performance in Alzheimer's disease: a PET imaging study with [(11)C]UCB-J. *Alzheimer's Dementia* 18, 2527–2536. <https://doi.org/10.1002/alz.12582>.
- Mecca, A.P., et al., 2022. Association of entorhinal cortical tau deposition and hippocampal synaptic density in older individuals with normal cognition and early Alzheimer's disease. *Neurobiol. Aging* 111, 44–53. <https://doi.org/10.1016/j.neurobiolaging.2021.11.004>.
- Michiels, L., et al., 2021. Synaptic density in healthy human aging is not influenced by age or sex: a [(11)C]UCB-J PET study. *Neuroimage* 232, 117877. <https://doi.org/10.1016/j.neuroimage.2021.117877>.
- O'Dell, R.S., et al., 2021. Association of Abeta deposition and regional synaptic density in early Alzheimer's disease: a PET imaging study with [(11)C]UCB-J. *Alzheimers. Res. Ther.* 13, 11. <https://doi.org/10.1186/s13195-020-00742-y>.
- Overhoff, F., et al., 2016. Automated spatial brain normalization and hindbrain white matter reference tissue gave improved [(18)F]-Florbetaben PET quantitation in Alzheimer's model mice. *Front. Neurosci.* 10, 45. <https://doi.org/10.3389/fnins.2016.00045>.
- Palop, J.J., Mucke, L., 2010. Amyloid-beta-induced neuronal dysfunction in Alzheimer's disease: from synapses toward neural networks. *Nat. Neurosci.* 13, 812–818. <https://doi.org/10.1038/nn.2583>.
- Palop, J.J., Mucke, L., 2016. Network abnormalities and interneuron dysfunction in Alzheimer disease. *Nat. Rev. Neurosci.* 17, 777–792. <https://doi.org/10.1038/nrn.2016.141>.
- Panda, R., et al., 2022. Disruption in structural-functional network repertoire and time-resolved subcortical fronto-temporoparietal connectivity in disorders of consciousness. *Elife* 11, e77462. <https://doi.org/10.7554/eLife.77462>.
- Pascoal, T.A., et al., 2021. Microglial activation and tau propagate jointly across Braak stages. *Nat. Med.* 27, 1592–1599. <https://doi.org/10.1038/s41591-021-01456-w>.
- Piacentini, R., et al., 2017. Reduced gliotransmitter release from astrocytes mediates tau-induced synaptic dysfunction in cultured hippocampal neurons. *Glia* 65, 1302–1316. <https://doi.org/10.1002/glia.23163>.
- Pike, V.W., 2009. PET radiotracers: crossing the blood-brain barrier and surviving metabolism. *Trends Pharmacol. Sci.* 30, 431–440. <https://doi.org/10.1016/j.tips.2009.05.005>.
- Quincozes-Santos, A., et al., 2021. Gliotoxicity and glioprotection: the dual role of glial cells. *Mol. Neurobiol.* 58, 6577–6592. <https://doi.org/10.1007/s12035-021-02574-9>.
- Ramirez, D.M.O., et al., 2025. Spontaneous pathology in PS19 tauopathy mice progresses via brain networks. *Neurobiol. Dis.* 215, 107072. <https://doi.org/10.1016/j.nbd.2025.107072>.
- Robbins, M., Clayton, E., Kaminski Schierle, G.S., 2021. Synaptic tau: a pathological or physiological phenomenon? *Acta Neuropathol. Commun.* 9, 149. <https://doi.org/10.1186/s40478-021-01246-y>.
- Roemer-Cassiano, S.N., et al., 2025. Amyloid-associated hyperconnectivity drives tau spread across connected brain regions in Alzheimer's disease. *Sci. Transl. Med.* 17, eadp2564. <https://doi.org/10.1126/scitranslmed.adp2564>.
- Rossi, R., Arjmand, S., Baerentzen, S.L., Gjedde, A., Landau, A.M., 2022. Synaptic vesicle glycoprotein 2A: features and functions. *Front. Neurosci.* 16, 864514. <https://doi.org/10.3389/fnins.2022.864514>.
- Salter, M.W., Beggs, S., 2014. Sublime microglia: expanding roles for the guardians of the CNS. *Cell* 158, 15–24. <https://doi.org/10.1016/j.cell.2014.06.008>.
- Schindelin, J., et al., 2012. Fiji: an open-source platform for biological-image analysis. *Nat. Methods* 9, 676–682. <https://doi.org/10.1038/nmeth.2019>.
- Selkoe, D.J., 2002. Alzheimer's disease is a synaptic failure. *Science* (1979) 298, 789–791. <https://doi.org/10.1126/science.1074069>.
- Song, X., et al., 2018. Mechanism of NMDA receptor channel block by MK-801 and memantine. *Nature* 556, 515–519. <https://doi.org/10.1038/s41586-018-0039-9>.
- Sosna, J., et al., 2018. Early long-term administration of the CSF1R inhibitor PLX3397 ablates microglia and reduces accumulation of intraneuronal amyloid, neuritic plaque deposition and pre-fibrillar oligomers in 5XFAD mouse model of Alzheimer's disease. *Mol. Neurodegener.* 13, 11. <https://doi.org/10.1186/s13024-018-0244-x>.
- Spangenberg, E.E., et al., 2016. Eliminating microglia in Alzheimer's mice prevents neuronal loss without modulating amyloid-beta pathology. *Brain* 139, 1265–1281. <https://doi.org/10.1093/brain/aww016>.
- Staurenghi, E., et al., 2021. Cholesterol dysmetabolism in Alzheimer's disease: a starring role for astrocytes? *Antioxidants* (Basel) 10, 1890. <https://doi.org/10.3390/antiox10121890>.
- Takkinen, J.S., et al., 2018. [(18)F]FMPEP-d2 PET imaging shows age- and genotype-dependent impairments in the availability of cannabinoid receptor 1 in a mouse model of Alzheimer's disease. *Neurobiol. Aging* 69, 199–208. <https://doi.org/10.1016/j.neurobiolaging.2018.05.013>.
- Toyonaga, T., Fesharaki-Zadeh, A., Strittmatter, S.M., Carson, R.E., Cai, Z., PET, 2022. Imaging of synaptic density: challenges and opportunities of synaptic vesicle glycoprotein 2A PET in small animal imaging. *Front. Neurosci.* 16, 787404. <https://doi.org/10.3389/fnins.2022.787404>.
- Tracy, T.E., et al., 2022. Tau interactome maps synaptic and mitochondrial processes associated with neurodegeneration. *Cell* 185, 712–728. <https://doi.org/10.1016/j.cell.2021.12.041> e714.
- Ullrich Gavilanes, E.M., et al., 2025. SV2A-PET imaging uncovers cortical synapse loss in multiple sclerosis. *Sci. Transl. Med.* 17. <https://doi.org/10.1126/scitranslmed.adt5585>.
- Vainchtein, I.D., Molofsky, A.V., 2020. Astrocytes and Microglia: In Sickness and in Health. *Trends Neurosci.* 43, 144–154. <https://doi.org/10.1016/j.tins.2020.01.003>.
- Vanderlinden, G., et al., 2022. Spatial decrease of synaptic density in amnesic mild cognitive impairment follows the tau build-up pattern. *Mol. Psychiatry* 27, 4244–4251. <https://doi.org/10.1038/s41380-022-01672-x>.
- Vogler, L., et al., 2023. Assessment of synaptic loss in mouse models of beta-amyloid and tau pathology using [(18)F]UCB-H PET imaging. *Neuroimage Clin.* 39, 103484. <https://doi.org/10.1016/j.nicl.2023.103484>.
- Wang, C., et al., 2022. Microglial NF-kappaB drives tau spreading and toxicity in a mouse model of tauopathy. *Nat. Commun.* 13, 1969. <https://doi.org/10.1038/s41467-022-29552-6>.
- Wang, J., et al., 2024. Tau pathology is associated with synaptic density and longitudinal synaptic loss in Alzheimer's disease. *Mol. Psychiatry* 29, 2799–2809. <https://doi.org/10.1038/s41380-024-02501-z>.
- Wang, J., et al., 2025. Prediction of longitudinal synaptic loss in Alzheimer's disease using tau PET and plasma biomarkers. *Alzheimers. Dement.* 21, e70333. <https://doi.org/10.1002/alz.70333>.
- Whiteside, D.J., et al., 2023. Synaptic density affects clinical severity via network dysfunction in syndromes associated with frontotemporal lobar degeneration. *Nat. Commun.* 14, 8458. <https://doi.org/10.1038/s41467-023-44307-7>.
- Wilson, D.M., et al., 2023. Hallmarks of neurodegenerative diseases. *Cell* 186, 693–714. <https://doi.org/10.1016/j.cell.2022.12.032>.
- Xiang, X., et al., 2021. Microglial activation states drive glucose uptake and FDG-PET alterations in neurodegenerative diseases. *Sci. Transl. Med.* 13, eabe5640. <https://doi.org/10.1126/scitranslmed.abe5640>.
- Yokoyama, M., Kobayashi, H., Tatsumi, L., Tomita, T., 2022. Mouse models of Alzheimer's disease. *Front. Mol. Neurosci.* 15, 912995. <https://doi.org/10.3389/fnmol.2022.912995>.
- Yoshiyama, Y., et al., 2007. Synapse loss and microglial activation precede tangles in a P301S tauopathy mouse model. *Neuron* 53, 337–351. <https://doi.org/10.1016/j.neuron.2007.01.010>.
- Zatcepin, A., et al., 2024. Regional desynchronization of microglial activity is associated with cognitive decline in Alzheimer's disease. *Mol. Neurodegener.* 19, 64. <https://doi.org/10.1186/s13024-024-00752-6>.
- Zhang, W., Xiao, D., Mao, Q., Xia, H., 2023. Role of neuroinflammation in neurodegeneration development. *Signal. Transduct. Target. Ther.* 8, 267. <https://doi.org/10.1038/s41392-023-01486-5>.